Comparison of surface radiative flux data sets over the Arctic Ocean

Jiping Liu,[1,2] Judith A. Curry,[1] William B. Rossow,[3] Jeffrey R. Key,[4] and Xuanji Wang[5]

Received 12 March 2004; revised 10 December 2004; accepted 3 January 2005; published 22 February 2005.

[1] Recent satellite data analysis and reanalysis projects have provided an unprecedented wealth of data sets relevant to surface energy budget in the Arctic Ocean. To assess how well we can reconstruct the variations of surface radiative fluxes used as boundary conditions to force sea ice models, the surface temperature, surface downwelling shortwave and longwave radiative fluxes of the (1) Cloud and Surface Parameter Retrieval (CASPR), (2) International Satellite Cloud Climatology Project (ISCCP-FD), (3) National Centers for Environmental Prediction Reanalysis II (NCEP-R2), and (4) European Centre for Medium-Range Weather Forecast 40-Year Reanalysis (ERA-40) were evaluated over the period November 1997 to September 1998. At the local scale the accuracy of these surface parameters was compared to the high-quality in situ measurements from the Surface Heat Budget of the Arctic Ocean (SHEBA) over the seasonal cycle and during particular storm events. The CASPR and NCEP-R2 are closer to the SHEBA for the surface temperature. The CASPR and ISCCP-FD are more accurate for the surface downward shortwave radiative fluxes. The ERA-40 agrees well with the SHEBA for the surface downward longwave radiative fluxes. At the basin scale the consistency of dominant spatial/temporal variability of these surface parameters across different data sets was examined. All data sets reproduce the patterns associated with the seasonal cycle, but they vary in their ability to capture patterns linked to synoptic variability.

Citation: Liu, J., J. A. Curry, W. B. Rossow, J. R. Key, and X. Wang (2005), Comparison of surface radiative flux data sets over the Arctic Ocean, *J. Geophys. Res.*, *110*, C02015, doi:10.1029/2004JC002381.

1. Introduction

[2] Climate model projections of future climate change show enhanced climate sensitivity at high latitudes, particularly in the Arctic [e.g., *Rind et al.*, 1995; *Randall et al.*, 1998; *Intergovernmental Panel on Climate Change*, 2001]. However, physical processes in the Arctic are not well understood in part due to the difficulties of acquiring observations [e.g., *Curry et al.*, 1996]. The main energy balance in the Arctic is between radiative energy loss and advective transport of warmer/moister air into the region. As the ocean surface cools, sea ice forms, which inhibits heat loss from the ocean, allowing the surface temperature to fall rapidly below the freezing point and reducing the radiative heat loss. The reduced surface heat loss is partly offset by the reduction of solar heating due to much higher snow/ice albedo. However, the persistent and extensive cloud cover in the Arctic has a net heating effect on the surface. Therefore the formation and melting of sea ice appears to be sensitive to the detailed surface radiative properties and the resultant radiative exchanges [e.g., *Ebert and Curry*, 1993]. To interpret the integrated effects of the radiative coupling between sea ice and the atmosphere, we need both high-quality surface flux observations covering the entire Arctic and models that accurately represent atmosphere-sea ice-ocean interactions.

[3] Presently, a diversity of sea ice models is used for operational sea ice forecasts, understanding physical processes, and studying climate variability and change [e.g., *Randall et al.*, 1998]. Sea ice models are often run in a stand alone mode to determine the role of different physical processes and to compare the performance of different sea ice models [e.g., *Curry et al.*, 2002]. Such applications require accurate atmospheric forcing specifications. Various simulation studies have specified the atmospheric forcings using climatology (i.e., the monthly mean state or daily values obtained by the interpolation between monthly mean values) from numerical weather forecast analyses, reanalyses or satellite-based products. However, several studies [e.g., *Zhang and Rothrock*, 1996; *Serreze et al.*, 1998] have suggested that the range of monthly average surface radiative fluxes in June among different data sets can be as large as $\sim$100 W/m^2 and $\sim$40 W/m^2 for the downwelling shortwave and longwave radiative fluxes respectively. Therefore uncertainties in atmospheric forcings are so large that it is difficult to determine whether discrepancies be-

[1]School of Earth and Atmospheric Sciences, Georgia Institute of Technology, Atlanta, Georgia, USA.
[2]Also at Key Laboratory for Polar Science, Polar Research Institute of China, Shanghai, China.
[3]NASA/Goddard Institute for Space Studies, New York, New York, USA.
[4]Office of Research and Applications, NOAA National Environmental Satellite, Data and Information Service, Madison, Wisconsin, USA.
[5]Cooperative Institute of Meteorological Satellite Studies, University of Wisconsin, Madison, Wisconsin, USA.

0148-0227/05/2004JC002381$09.00

tween simulated and observed sea ice properties arise from deficiencies in atmospheric forcings or from the formulations of sea ice models.

[4] Toward addressing this issue, *Curry et al.* [2002] assessed the sensitivity of sea ice simulations to errors in different atmospheric forcing data sets using a single-column ice thickness model. Since then, several recent satellite data analysis and reanalysis projects have produced an unprecedented wealth of data sets for such comparisons on high temporal resolution at both local and basin scales. In this paper, we extend Curry's study to evaluate the accuracy of atmospheric forcings in new high spatial resolution satellite-derived products and newly released reanalyses against field measurements at the local scale. Furthermore, we evaluate the consistency of dominant spatial/temporal variability of atmospheric forcings for these data sets at the basin scale.

[5] Another critical issue in atmospheric forcings for sea ice models is the importance of the timing of particular meteorological events for the sea ice evolution. As demonstrated by the Surface Heat Budget of the Arctic Ocean experiment (SHEBA) [*Perovich et al.*, 1999], sea ice is particularly sensitive to variations in atmospheric forcings during key periods. For example, a storm in late July 1998 produced substantial ice divergence, opening of leads and mixing in the upper ocean, which led to autumnal freezing in a manner different from climatology. Therefore knowing the monthly or seasonal mean state of atmospheric forcings is not sufficient to understand atmosphere-sea ice-ocean interactions. Individual meteorological events can have irreversible effects on sea ice. To provide a credible prediction concerning the stability of pack ice in the Arctic, an evaluation of how well we can reconstruct the synoptic variations of atmosphere forcings is needed.

2. Description of Data Sets

[6] To force sea ice models, the following atmospheric parameters are generally required: (1) surface air temperature, humidity and density; (2) downwelling shortwave and longwave radiative fluxes at the surface; (3) precipitation; and (4) surface wind speed and direction. This paper focuses specifically on the surface radiative fluxes.

[7] To evaluate the large-scale analyses obtained from satellites and reanalyses, we use in situ data obtained from the SHEBA [*Perovich et al.*, 1999; *Uttal et al.*, 2002]. Measurements during the SHEBA were obtained from 2 October 1997 through 10 October 1998. During that period a Canadian icebreaker frozen into ice floes was used as a base for scientific studies of the atmosphere, ice and ocean. Research aircraft from the United States and Canada also took part in the experiment during the spring and summer of 1998. The SHEBA experiment has arguably provided the highest quality and most comprehensive suite of surface properties and radiative fluxes ever made in the Arctic Ocean. The hourly surface skin temperature, air temperature at 2.5 m, and surface downwelling shortwave and longwave radiative fluxes were used in this study (see *Persson et al.* [2002] for detailed discussions regarding the SHEBA flux data and its reliability).

[8] Using the SHEBA data, we evaluated two satellite-based products and two newly released numerical weather prediction reanalyses: (1) the Cloud and Surface Parameter Retrieval/Arctic Region Climate Model Intercomparison Project (CASPR/ARCMIP); (2) the International Satellite Cloud Climatology Project/Arctic Region Climate Model Intercomparison Project (ISCCP-FD/ARCMIP); (3) the National Centers for Environmental Prediction–Atmospheric Model Intercomparison Project Reanalysis II (NCEP-R2); and (4) the European Centre for Medium-Range Weather Forecast 40-Year Reanalysis (ERA-40).

[9] The CASPR/ARCMIP data set includes subsets of the SHEBA AVHRR (Advanced Very High Resolution Radiometer) 5 km (the western Arctic) and 25 km (the entire Arctic) retrievals regridded onto a 50 km equal area scalable Earth coordinate (EASE, see http://nsidc.org/data/ease for details). The CASPR/ARCMIP includes the all sky surface skin temperature, broadband surface albedo, cloud properties and surface radiative fluxes. The calculation of cloudy sky surface skin temperature is based upon an empirical relationship between the clear sky surface skin temperature, wind speed, and solar zenith angle. The surface radiative fluxes are computed using the FluxNet (the neural network version of Streamer, a radiative transfer model [*Key and Schweiger*, 1998]). Also, see *Key* [2001] for more information on the algorithms and their validation. The time period for the CASPR/ARCMIP is from 1 January 1997 through 31 December 1998, which spans the entire SHEBA experiment. Twice-daily data are available at 0400 and 1400 LT.

[10] The ISCCP-FD/ARCMIP data set is a subset of ISCCP-FD flux product regridded onto a 50 km resolution EASE grid. The ISCCP-FD/ARCMIP includes the surface and top of atmosphere radiative fluxes, and important physical quantities used to calculate them. The radiative fluxes are calculated using a radiative transfer model, which simulates the effects of absorption by ozone and multiple scattering by aerosol, molecules, and clouds in the atmosphere [*Zhang et al.*, 2004]. This data set covers the time period from 1 September 1997 to 30 September 1998, which is roughly coincident with that of the SHEBA project. The spatial coverage spans 55°N to the North Pole. The temporal resolution is every 3 hours (eight times per day). More information on the ISCCP-FD analysis project can be found at http://isccp.giss.nasa.gov/projects/flux.html.

[11] The NCEP-R2 and ERA-40 global reanalyses are provided four times per day. The NCEP-R2 is on a T62 Gaussian grid with 192 (longitude) by 94 (latitude) points, from 1979 to present. The NCEP-R2 fixed the known processing errors in the original NCEP/NCAR (National Center for Atmospheric Research) reanalysis and improved the parameterizations of some physical processes. Relevant to the northern high latitudes, improvements include (1) fixed problems in snow cover, humidity diffusion and ocean albedo and (2) better parameterizations for the planetary boundary layer, shortwave radiation, convection, cloud top cooling and cloud-tuning coefficients (see *Kanamitsu et al.* [2002a, 2002b] for a detailed summary of these and other improvements). The spatial resolution of the ERA-40 is 2.5° by 2.5°, covering the time period from September 1957 to October 2002. The ERA-40 also corrected some problems in the previous ERA-15 (December 1978 to February 1994)

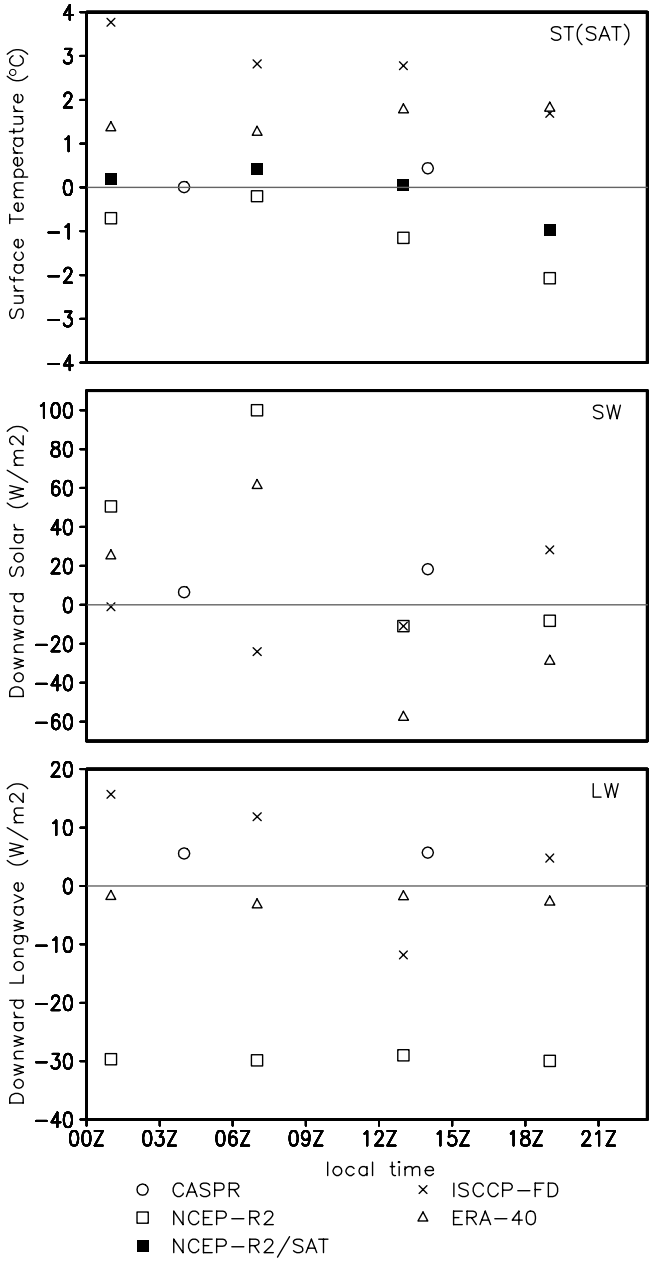

Figure 1. Differences by time of day for the (top) surface skin (air) temperature (°C), (middle) surface downwelling shortwave radiative fluxes (W/m^2), and (bottom) surface downwelling longwave radiative fluxes (W/m^2) over the entire period of the Cloud and Surface Parameter Retrieval (CASPR), International Satellite Cloud Climatology Project (ISCCP-FD), National Centers for Environmental Prediction Reanalysis II (NCEP-R2), and European Centre for Medium-Range Weather Forecast 40-Year Reanalysis (ERA-40) analyses relative to the Surface Heat Budget of the Arctic Ocean (SHEBA) data.

such as the severe cold bias in the surface and near-surface temperatures during winter and spring in the northern high latitude through improved parameterizations (i.e., soil freezing, surface snow cover and sea ice). The temporal consistency of the ERA-40 on synoptic timescales is better than the earlier ERA-15 (see http://www.ecmwf.int/research/era for more on the merits of the ERA-40).

3. Evaluation of Data Sets Using In Situ Observations (Pixel Comparisons)

[12] The time period used in the following comparisons is 1 November 1997 to 31 September 1998. We evaluated the surface skin/air temperature (ST/SAT), surface downwelling shortwave (SW) and longwave (LW) radiative fluxes of the CASPR, ISCCP-FD, NCEP-R2 and ERA-40 against the SHEBA field measurements. The CASPR, ISCCP and NCEP-R2 surface skin temperature was compared with the SHEBA surface skin temperature, since the CASPR surface air temperature is not available. The NCEP-R2 and ERA-40 air temperature at 2 m was compared with the SHEBA air temperature at 2.5 m, since the ERA-40 surface skin temperature is not available. The SHEBA hourly data shows that the surface skin temperature is on average slightly colder (~0.4°–0.6°C) than the 2.5 m air temperature. Our inquiries (K. Masao, J. Woollen, and D. Moritz, personal communication, 2004) suggested that the SHEBA radiosonde data (wind, temperature and humidity profiles) were assimilated into the reanalyses (NCEP-R2 and ERA-40), which kept the overall thermodynamic state of the reanalyses (i.e., surface temperature as shown below) fairly close to the SHEBA observations, and would tend to increase the accuracy of other variables of the reanalyses at the SHEBA site as well. However, the main thing we are evaluating is the surface radiative fluxes, which depend not only on the temperature and humidity profiles, but also on the model parameterizations (i.e., clouds, aerosols and ozone). This means that the model parameterizations are the main cause of biases found in the surface radiative fluxes for the reanalyses as compared with the SHEBA data as shown below.

3.1. Seasonal Cycle

[13] A comparison of the CASPR, ISCCP-FD, NCEP-R2 and ERA-40 analyses with the SHEBA field measurements is shown in Table 1 (seasonal cycle) and Figure 1 (diurnal cycle). During the SHEBA experiment, the surface consisted of dry snow in April and May. Most of the snowmelt occurred during the first two weeks of June. Melt ponds formed in early June and continued to develop into August. Beginning on 12 August, the melt ponds began to freeze. Snow began to accumulate on the ice in late August and by mid-September the snow cover was roughly 10 cm deep. Because the variations of the atmospheric parameters depend on the surface characteristics, we divided the entire period into five subperiods: November–February (NDJF), dry snow (DS: 1 March–25 May), snowmelt (SM: 26 May–9 June), melt ponds (MP: 10 June–1 August) and fall freeze-up (FFU: 2 August–30 September) based on the above observations. In Table 1, statistics (relative to the SHEBA data) including bias, standard deviation (std), and correlation coefficient (corr) over the entire period and five subperiods are given for the average over 0100, 0700, 1300 and 1900 LT (consistent with the time resolution of the reanalyses), except over 0400 and 1400 LT for the CASPR.

[14] The surface skin temperature comparisons show that the CASPR and ISCCP-FD values are warmer than the

Table 1. Comparison of the Surface Skin (Air) Temperature of the Cloud and Surface Parameter Retrieval (CASPR), International Satellite Cloud Climatology Project (ISCCP-FD), National Centers for Environmental Prediction Reanalysis II (NCEP-R2), and European Centre for Medium-Range Weather Forecast 40-Year Reanalysis (ERA-40) Analyses With the Surface Heat Budget of the Arctic Ocean (SHEBA) Data[a]

	ST (SAT), °C				
Period	SHEBA	CASPR	ISCCP-FD	NCEP-R2	ERA-40
Entire (1 Nov.–30 Sep.)					
Bias		0.2	2.8	−1.0 (−0.1)	1.6
Std	13.7 (13.5)	11.9	9.7	13.1 (12.9)	12.7
Corr		0.97	0.92	0.97 (0.98)	0.99
NDJF (1 Nov.–28 Feb.)					
Bias		2.1	6.8	−0.9 (−0.3)	1.5
Std	8.3 (8.1)	6.2	3.6	7.6 (7.3)	7.2
Corr		0.88	0.47	0.89 (0.91)	0.94
DS (1 March–25 May)					
Bias		−0.2	2.9	−1.0 (−0.1)	1.9
Std	7.3 (7.0)	6.0	4.9	6.7 (6.6)	6.3
Corr		0.87	0.67	0.83 (0.88)	0.94
SM (26 May–9 June)					
Bias		−2.1	−1.8	−1.0 (−0.2)	0.9
Std	1.4 (1.5)	2.3	2.0	1.4 (1.)	1.3
Corr		0.20	0.15	0.63 (0.64)	0.86
MP (10 June–1 Aug.)					
Bias		−0.4	−1.1	−0.6 (0.3)	1.2
Std	0.7 (1.4)	1.6	2.1	1.4 (1.1)	0.7
Corr		0.11	0.14	0.59 (0.72)	0.77
FFU (2 Aug.–30 Sep.)					
Bias		−1.8	−2.7	−1.8 (0.7)	0.4
Std	2.3 (2.2)	3.1	2.6	3.5 (4.2)	2.8
Corr		0.67	0.41	0.71 (0.75)	0.94

[a]Abbreviations are as follows: ST (SAT), surface temperature (skin/air temperature); NDJF, November–February; DS, dry snow; SM, snowmelt; MP, melt ponds; FFU, fall freeze-up; std, standard deviation; corr, correlation coefficient.

SHEBA values over the entire period (Table 1). The ISCCP-FD values are too warm (2.8°C) for the entire period, which is a balance of large warm biases during the November–February and dry snow periods, and large cold biases during the snowmelt, melt pond and fall freeze-up periods. The CASPR values have the smallest bias (0.2°C) for the entire period, resulting from a cancellation of the warm bias during the November–February period and cold biases during dry snow, snowmelt, melt pond and fall freeze-up periods. By contrast, the NCEP-R2 values are colder (−1°C) than the SHEBA values for the entire period, which is persistent for all surface characteristics. The magnitude of the biases in the CASPR and NCEP-R2 is much smaller than that of the variability (except during the snowmelt period), but the magnitude of the biases in the ISCCP-FD is larger than that of the variability during the November–February and fall freeze-up periods. Comparisons of air temperature show little biases in the NCEP-R2 for the entire and all subperiods. The ERA-40 values are substantially warmer (1.6°C) than the SHEBA values for the entire period, which is persistent for all surface characteristics (Table 1). The magnitude of the biases in the NCEP-R2 and ERA-40 is smaller than that of the variability for all subperiods. Figure 1 shows the differences between the various data sets and the SHEBA data by time of day for the entire period. The fact that the differences of a specific data set are nearly the same all day means that data set has the same diurnal cycle as the SHEBA (but it may be biased). It appears that all data sets have a similar diurnal cycle of the surface temperature as the SHEBA, since the differences between the various data sets and the SHEBA show no particular dependence on time of day. However, the CASPR and NCEP-R2 have smaller differences all day than the ISCCP-FD and ERA-40. Overall, the CASPR and NCEP-R2 surface temperatures are closer to the SHEBA measurements.

[15] Comparison of the surface downwelling shortwave radiation shows that the CASPR and NCEP-R2 values have positive biases over the entire periods, which are persistent for all surface characteristics (Table 2). The NCEP-R2 values are systematically too large; the biases can be greater than ∼70 W/m^2 during the melt season. The ISCCP-FD values show small negative bias over the entire period, which is a balance of negative biases during the November–February, dry snow and snowmelt periods, and positive biases during the melt pond and fall freeze-up periods. The ERA-40 values have the smallest biases for the entire and all subperiods. The magnitude of the biases in the CASPR, ISCCP-FD and ERA-40 is smaller than that of the variability for all subperiods, but the magnitude of the biases in the NCEP-R2 is larger than that of the variability during the melt season. The differences by time of day for the NCEP-R2 and ERA-40 show a large variation than the CASPR and ISCCP-FD (Figure 1), which suggests that the satellite-based products has more accurate diurnal cycle of the downwelling shortwave radiative fluxes than the reanalyses. The smallest bias in the ERA-40 as shown in Table 2 is actually a cancellation of large positive biases (at 0100 and 0700 LT) and large negative biases (at 1300 and 1900 LT). By contrast, the CASPR and ISCCP-FD show persistent

Table 2. Comparison of the Downwelling Shortwave Radiative Fluxes of the CASPR, ISCCP-FD, NCEP-R2, and ERA-40 Analyses With the SHEBA Data[a]

	SW, W/m^2				
Period	SHEBA	CASPR	ISCCP-FD	NCEP-R2	ERA-40
Entire (1 Nov.–30 Sep.)					
Bias		12.5	−1.9	32.9	0.2
Std	115.8	136.2	113.2	113.9	113.0
Corr		0.95	0.88	0.93	0.92
NDJF (1 Nov.–28 Feb.)					
Bias		−0.1	−0.6	0.3	∼0.0
Std	2.4	1.5	1.4	3.3	2.3
Corr		0.99	0.96	0.86	0.84
DS (1 March–25 May)					
Bias		10.8	−34.6	35.6	8.7
Std	95.9	109.5	91.4	109.7	106.2
Corr		0.95	0.81	0.93	0.93
SM (26 May–9 June)					
Bias		40.7	−24.1	85.1	5.0
Std	52.4	53.3	72.0	47.1	57.1
Corr		0.41	0.24	0.30	0.38
MP (10 June–1 Aug.)					
Bias		23.1	14.8	72.4	−8.5
Std	92.9	72.3	76.1	64.0	63.6
Corr		0.74	0.54	0.66	0.66
FFU (2 Aug.–30 Sep.)					
Bias		19.0	26.7	44.2	−6.2
Std	49.9	61.1	68.6	74.4	51.4
Corr		0.87	0.71	0.83	0.82

[a]SW, downwelling shortwave radiative fluxes.

Table 3. Comparison of the Downwelling Longwave Radiative Fluxes of the CASPR, ISCCP-FD, NCEP-R2, and ERA-40 Analyses With the SHEBA Data[a]

	LW, W/m^2				
Period	SHEBA	CASPR	ISCCP-FD	NCEP-R2	ERA-40
Entire (1 Nov.–30 Sep.)					
Bias		5.6	5.1	−29.6	−2.3
Std	62.4	56.2	41.0	58.0	25.7
Corr		0.91	0.60	0.90	0.92
NDJF (1 Nov.–28 Feb.)					
Bias		13.1	39.1	−22.5	−5.8
Std	43.8	39.3	28.3	39.7	42.5
Corr		0.78	−0.13	0.85	0.88
DS (1 March–25 May)					
Bias		5.8	9.7	−35.1	−10.0
Std	37.7	36.0	31.2	32.8	36.9
Corr		0.67	0.11	0.63	0.67
SM (26 May–9 June)					
Bias		−5.6	−17.1	−40.6	−0.8
Std	25.8	21.9	30.4	29.1	20.5
Corr		0.54	0.12	0.56	0.53
MP (10 June–1 Aug.)					
Bias		1.3	−15.7	−29.7	11.5
Std	30.0	28.6	32.3	29.6	14.6
Corr		0.73	0.41	0.56	0.41
FFU (2 Aug.–30 Sep.)					
Bias		−2.7	−23.1	−32.95	1.5
Std	21.8	32.1	27.9	32.4	18.4
Corr		0.64	0.31	0.56	0.57

[a]LW, downwelling longwave radiative fluxes.

smaller biases all day than the NCEP-R2 and ERA-40. Overall, the CASPR and ISCCP-FD values are more accurate for the surface downwelling shortwave radiative fluxes.

[16] The surface downwelling longwave radiation comparisons suggest that the CASPR and ISCCP-FD values have positive biases (5.6 W/m^2 and 5.1 W/m^2) over the entire period (Table 3), resulting from a balance of positive biases during the November–February and dry snow periods and negative biases during the snowmelt, melt pond and fall freeze-up periods. The NCEP-R2 values show substantially negative biases (−29.6 W/m^2) for the entire period, which is persistent for all surface characteristics. The ERA-40 values have the smallest bias for the entire period, albeit due to a cancellation between small negative biases in the November–February, dry snow and snowmelt periods with small positive biases in the melt pond and fall freeze-up periods (opposite to the CASPR and ISCCP-FD). The magnitude of the biases in the CASPR and ERA-40 is smaller than that of the variability for all subperiods, but the opposite is the case for the NCEP-R2. The magnitude of the biases in the ISCCP-FD is comparable to that of the variability during the November–February and fall freeze-up periods. All data sets (except the ISCCP-FD) show nearly the same differences all day for the downwelling longwave radiative fluxes. Among them, the ERA-40 has the smallest differences all day (Figure 1). Overall, the ERA-40 values give the best statistics for the surface downwelling longwave radiative fluxes.

3.2. Storm Event Comparisons

[17] During SHEBA, the onset of surface snowmelt was triggered by liquid precipitation from a storm on 29 May 1998. The rain caused melt metamorphosis of the surface snow, which reduced the surface albedo, increased the absorbed solar radiation and accelerated snowmelt. Thus snowmelt occurred one month earlier than expected from the climatology. On 30 July 1998, another storm triggered the freeze-up of the surface melt ponds, allowing snow accumulation on the surface, increasing the surface albedo and freezing the melt ponds. Therefore the melt season at the SHEBA site was initiated in late spring and terminated in late summer directly by these two synoptic events. Thus the variations of the atmospheric parameters associated with particular storm events are critical to sea ice seasonal evolution. It is therefore necessary to examine the accuracy of the atmospheric parameters in different data sets associated with the timing and strength of storm effects. We analyzed the above two storm events as well as another in the middle of the melt season (4 July 1998).

[18] As these storms moved over the SHEBA site, the surface pressure dropped by ~25, 12 and 18 hpa within ~3 days and reached minimum values on 29 May, 4 July, and 31 July, respectively (Figure 2 (top row)). The variations of the surface skin/air temperature, and surface downwelling shortwave and longwave radiative fluxes through these storm events are demonstrated in Figure 2 (rows 2–4). Comparisons of the surface skin/air temperature suggest that the CASPR values are systematically low (always below the freezing point), and cannot reproduce the observed temperature variations for all storm events. The ISCCP-FD values show extremely large variability during the melt season that exceeds the variability for SHEBA and other data sets. Both the NCEP-R2 and ERA-40 well capture the real temperature variations through the 29 May and 31 July storms. The NCEP-R2 values exhibit larger variability than the SHEBA data during the strengthening of the 4 July storm, while the ERA-40 values cannot capture the observed temperature variations and show positive biases (always above the freezing point) during the 4 July storm. Therefore the NCEP-R2 values well represent the variations of both the surface skin temperature (as compared with the CASPR and ISCCP-FD) and air temperature (as compared with ERA-40) during all storm events. Owing to the assimilation of the SHEBA radiosonde data in the reanalyses, the surface temperature variability of the reanalyses appears to be much better than that of the satellite-based products, which also suggests that in areas where there are no data to assimilate (most of the Arctic Ocean), the surface temperature probably contain larger errors than at the SHEBA site.

[19] For the surface downwelling shortwave radiation of the SHEBA observations, the most prominent feature (other than the diurnal cycle due to the change of the solar zenith angle) is a decrease with the strengthening of the storm and an increase with the weakening of the storm (Figure 2). In general, enhanced (reduced) cyclonic activity results in more (less) mid/upper level clouds, which have larger cloud water content and smaller cloud drop size, leading to reduced (enhanced) solar radiation at the surface [e.g., *Curry et al.*, 1996]. Comparisons of the downwelling solar radiation show that the minimum values of the CASPR are systematically larger than the SHEBA data and have little variation for the peak values across the storms. The ISCCP-FD, NCEP-R2 and ERA-40 well represent the observed solar variability, but the NCEP-R2 and ERA-40 seem to lag the SHEBA data by a few hours and the minimum (peak)

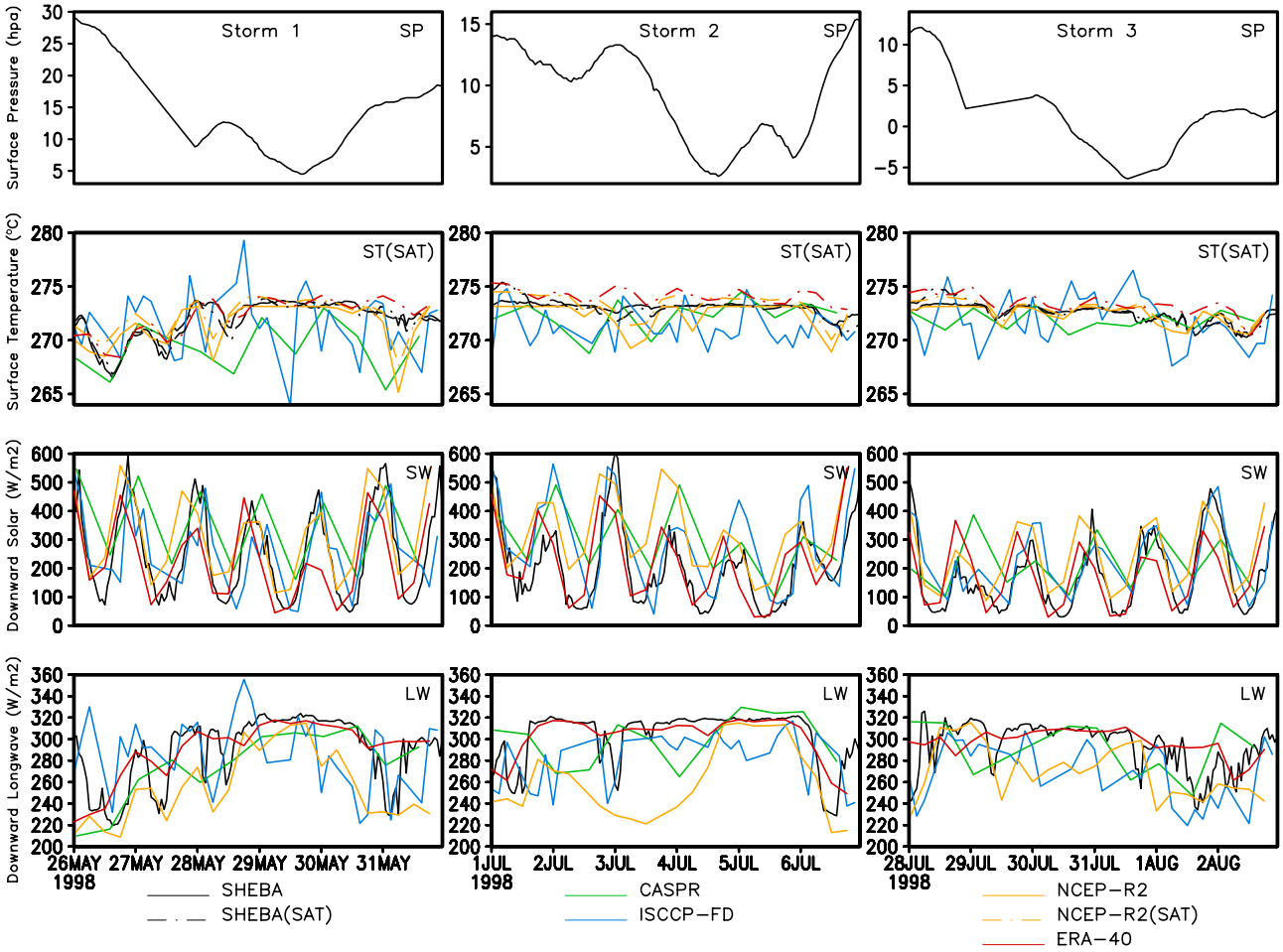

Figure 2. Variations of the (top) surface pressure (hpa), (top middle) surface skin (air) temperature (°C), (bottom middle) surface downwelling shortwave radiative fluxes (W/m^2), and (bottom) surface downwelling longwave radiative fluxes (W/m^2) of the CASPR, ISCCP-FD, NCEP-R2, and ERA-40 analyses through three storm events (29 May, 4 July, and 31 July) at the SHEBA site.

values in the NCEP-R2 (ERA-40) are systematically larger (smaller) than the SHEBA data. Therefore the ISCCP-FD most closely matches the SHEBA observations (note that all data sets capture the diurnal cycle).

[20] The surface downwelling longwave radiation of the SHEBA data vary around 300 W/m^2 under cloudy sky conditions, with the sharp decreases in the flux values corresponding to clear sky conditions. Sensitivity studies suggested that cloud fraction/thickness and air temperature are the dominant factors in the determination of the surface downward longwave fluxes [*Zhang et al.*, 1995, 2004; *Chiacchio and Francis*, 2002]. Since the Arctic clouds are frequently thin (with emissivity less than 1), the downwelling longwave fluxes are also sensitive to liquid/ice content and particle size [e.g., *Curry et al.*, 1996]. Compared with the SHEBA observations, the NCEP-R2 values have systematically negative biases (which is also consistent with its low biases in the surface temperature and high biases in the downward solar radiation) and cannot realistically produce the observed longwave variability for the 4 July storm. The CASPR (except for the 29 May storm) and ISCCP-FD capture the observed longwave variations to some degree, particularly some transitions between the cloudy and clear sky conditions, but show excessive variations under the cloudy conditions. The ERA-40 resembles the SHEBA observations closely, albeit with a more smooth time series.

4. Basin-Scale Comparisons

[21] To determine if the primary characteristics of regional spatial/temporal variability in the surface skin/air temperature and downwelling solar and longwave radiative fluxes are consistent across different data sets during the SHEBA period, an empirical orthogonal function analysis (EOF) was employed. Because the CASPR, ISCCP-FD, NCEP-R2 and ERA-40 analyses have different temporal and spatial resolutions, before performing the EOF analysis, we interpolated each data sets to the same time resolution (four times daily, consistent with the reanalyses) and to the same spatial resolution on a 100 km resolution EASE grid. The interpolation also filled in missing values in the CASPR and ISCCP-FD data sets.

4.1. Seasonal Cycle

[22] Figures 3 and 4 show the first loading patterns (EOFs) and their principal components (PCs) of the

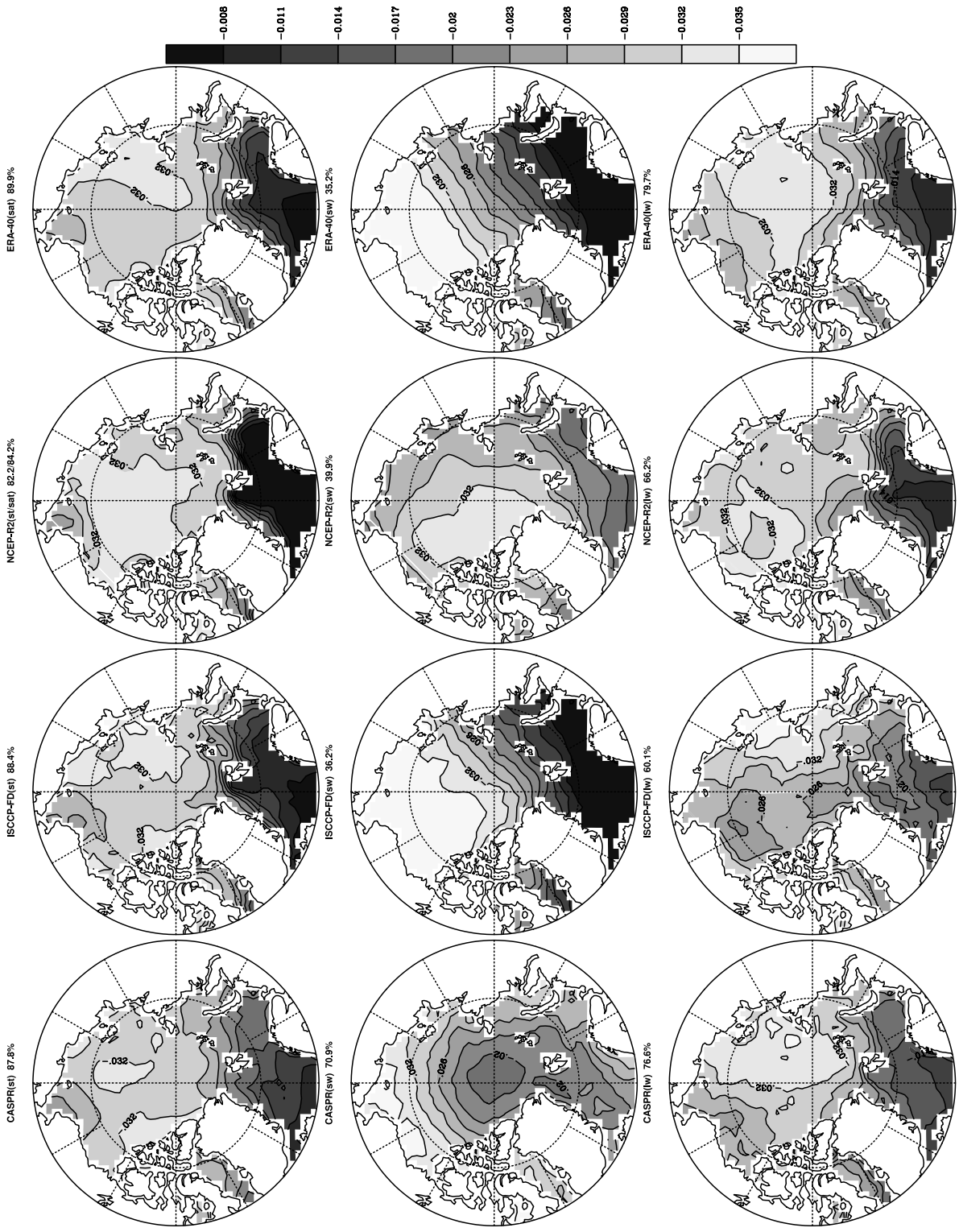

Figure 3. First principal component loading patterns of the interpolated surface skin (air) temperature and the downwelling shortwave and longwave radiative fluxes of the CASPR, ISCCP-FD, NCEP-R2, and ERA-40 analyses over the ocean north of 65°N.

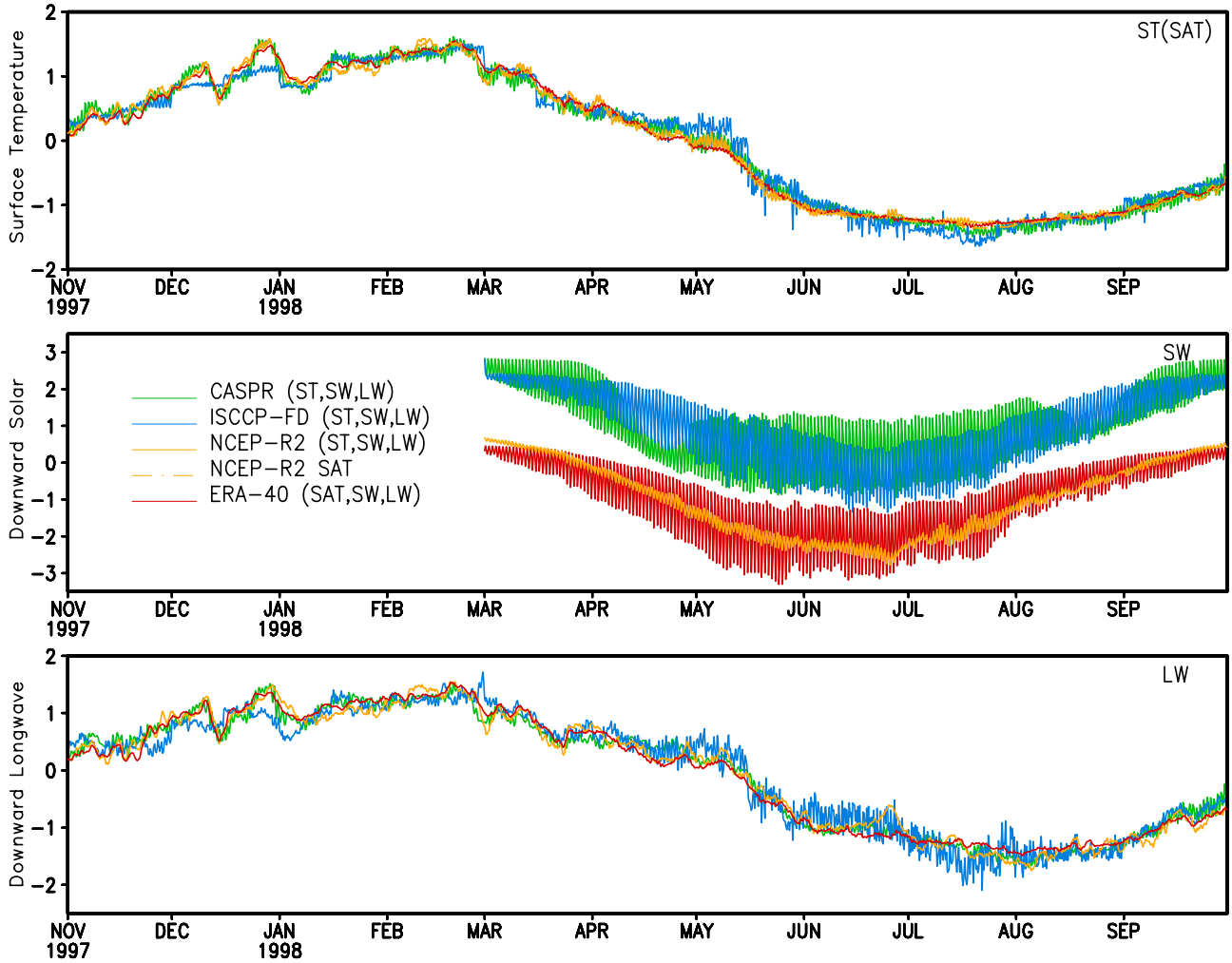

Figure 4. Standardized principal components (or scores) corresponding to the first empirical orthogonal function (EOF) modes in Figure 3. (Note that the downward shortwave radiative fluxes of the CASPR/ISCCP-FD and the NCEP-R2/ERA40 are shifted up and down by one standard deviation, respectively, for better visualization.)

CASPR, ISCCP-FD, NCEP-R2 and ERA-40 analyses over the ocean north of 65°N, which explain the majority of the total variance. Each pair EOF/PC describes a mode. The EOFs identify regions that are closely related and with strong gradient (spatial variability). The PCs indicate the amplitude of each EOF as it varies through time (temporal variability). Because the first EOFs are negative everywhere, the positive (negative) values of the corresponding PCs indicate cold (warm) anomalies, and reduced (enhanced) downward solar and longwave radiative fluxes. Thus the first load patterns appear to be the seasonal cycle, associated with the warming in summer and cooling in winter. Comparisons of the surface temperature suggest that all data sets exhibit large (small) temperature variability in the Arctic Ocean (Greenland-Iceland-Norwegian (GIN) Seas) and an intense temperature gradient in the northern Greenland and Norwegian Seas, representing the sea ice edge zones. However, the maximum temperature variability is more toward North America (Siberia) in the CASPR and NCEP-R2 (the ISCCP-FD and ERA-40). The downward solar radiation comparisons show that the ISCCP-FD, NCEP-R2 and ERA-40 have a gradually increasing solar variability from the GIN Seas to the Beaufort and Chukchi Seas, except that the maximum solar variability in the NCEP-R2 is more toward the Canadian Archipelago and the gradient is weak in the GIN Seas. By contrast, the CASPR has a reversed gradient from the GIN Seas to the North Pole, and its first EOF mode accounts for almost twice the total variance explained by others. For the downward longwave radiative fluxes, all data sets exhibit spatial structures similar to that of the surface temperature. However, the longwave variability contrast is weaker between the Arctic Ocean and the GIN Seas in the ISCCP-FD than in other data sets. In general, the dominant basin-scale patterns associated with the seasonal cycle are consistent across different data sets (except the downward solar radiation in the CASPR), which is also supported by high correlations between the principal components of each atmospheric parameter across different data sets (0.97–0.99 for the surface temperature and longwave radiation,

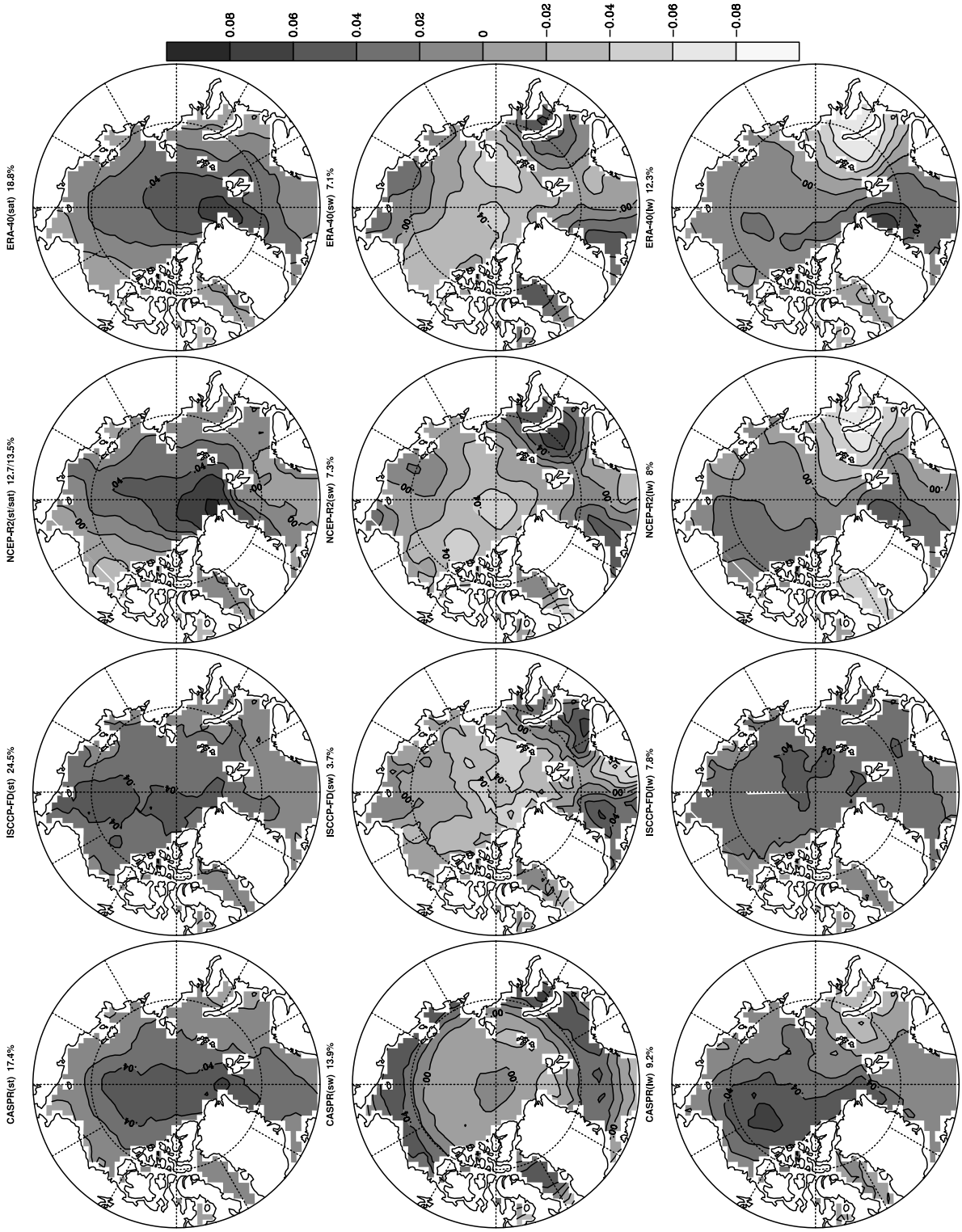

Figure 5. First principal component loading patterns (EOFs) of the residual interpolated surface skin (air) temperature and the downwelling shortwave and longwave radiative fluxes of the CASPR, ISCCP-FD, NCEP-R2, and ERA-40 analyses after removing the seasonal cycle.

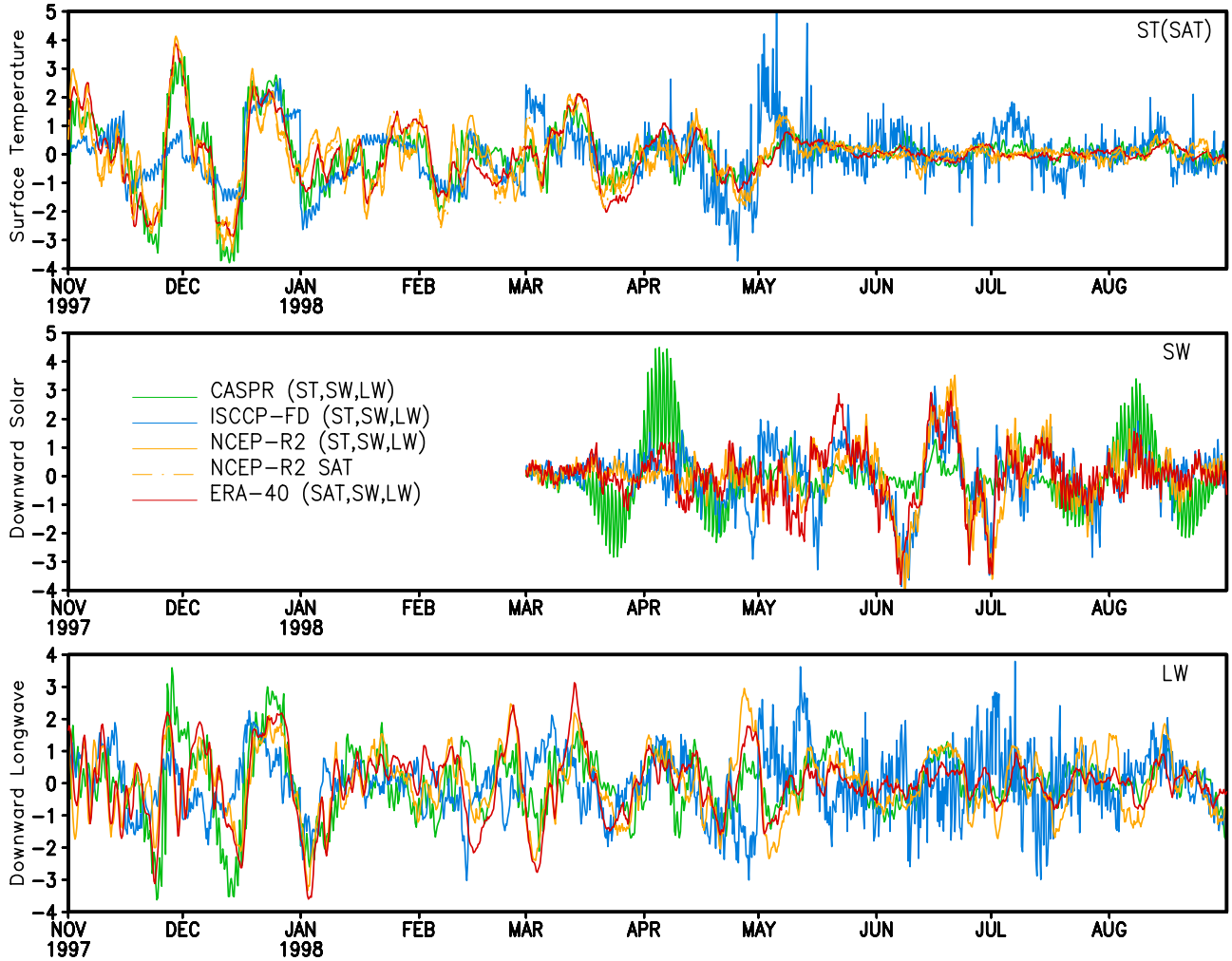

Figure 6. Standardized principal components (or scores) corresponding to the first EOF modes in Figure 5.

0.85–0.89 for solar radiation (except 0.46–0.79 for the CASPR)).

4.2. Synoptic Variability

[23] Are the dominant covarying spatial patterns in the Arctic Ocean at the synoptic timescale (beyond the seasonal cycle) consistent across different data sets? To answer this question, we removed the seasonal cycle (30 day running average) from the interpolated surface temperature, downward solar and longwave radiative flux time series in each grid cell, before repeating the EOF analysis on the residual data sets. Figures 5 and 6 show the first EOF modes and their principal components for the residual data sets. Comparisons of the surface temperature show that all data sets exhibit large temperature variability near Fram Strait that decreases toward the surrounding sub-Arctic seas, while the ISCCP-FD can not capture the decrease in the Beaufort and Chukchi Seas. The corresponding principal components demonstrate large fluctuations at the synoptic timescale from November to May and very small fluctuations from June to September (since the surface temperature stays around the freezing point in summer). For the downward shortwave radiation, the ISCCP-FD, NCEP-R2 and ERA-40 show an out of phase relationship between the interior Arctic Ocean, and the Greenland, Barents, Kara and Chukchi Seas, which is not present in the CASPR. The downward longwave radiation comparisons show that the CASPR, NCEP-R2 and ERA-40 exhibit a dipole pattern between (1) the Barents and Kara Seas and (2) the Greenland Sea and eastern Arctic Ocean, while the ISCCP-FD has positive values everywhere. The longwave principal components demonstrate very large fluctuations at the synoptic timescale for the entire period. Not surprisingly, removing the seasonal cycle results in lower correlations between the principal components of each atmospheric parameter across different data sets, though two reanalyses still maintain high correlations. The correlation of the surface temperature between the CASPR and the reanalyses is much higher than that between the ISCCP-FD and reanalyses. The CASPR has insignificant correlation with other data sets for the downward solar radiation, while the ISCCP-FD likewise has negligible correlation with others for the downward longwave radiation (Table 4).

[24] In an attempt to interpret the spatial patterns in the above first EOF modes associated with the synoptic variability, we conducted EOF analysis on the residual NCEP-

Table 4. Correlations Between the Principal Components of the Various Data Sets for Each Atmospheric Parameter After Removing the Seasonal Cycle

Correlation	CASPR	ISCCP-FD	NCEP-R2	ERA-40
CASPR				
ST (SAT)	1	0.46	0.78 (0.78)	(0.86)
SW	1	0.17	0.18	0.19
LW	1	0.14	0.56	0.59
ISCCP-FD				
ST (SAT)		1	0.37 (0.39)	(0.42)
SW		1	0.62	0.56
LW		1	0.01	0.11
NCEP-R2				
ST (SAT)			1 (0.96)	0.86 (0.91)
SW			1	0.78
LW			1	0.83
ERA-40				
SA (SAT)				1
SW				1
LW				1

R2 sea level pressure (SLP, after removing 30 day running average). The climatological basin-scale circulation in the Arctic is characterized by an anticyclonic regime (the Beaufort high) and a cyclonic regime (the Icelandic low), with the Transpolar Drift Stream (TDS) in between. The first three leading EOF modes of the NCEP-R2 SLP (explaining ~64% of the total variance) reflect the variability of these climatological features at the synoptic scale (Figure 7). They are characterized by (1) a large pressure variability near north of the Kara Sea that decreases toward the eastern Arctic (ESLP1); (2) an out of phase relationship between the Arctic Ocean (between 90°E and 120°W) and the GIN Seas (ESLP2); and (3) a dipole pattern between the Barents Sea and the Canadian Archipelago (ESLP3). Associated with positive (negative) values of the principal component, the ESLP1 favors anomalous southerlies (northerlies) at Fram Strait, leading to strong (weak) ice export (the opposite is case for the ESLP3), which is responsible for the aforementioned large temperature variability at Fram Strait at the synoptic scale (Figure 5). The correlations in Table 5 also support this explanation. The ESLP1 has high correlation with the first EOF mode of the downward solar radiation (0.45). Linked to positive (negative) values of the principal component, the ESLP1 favors advection of cold/dry (warm/moist) air from the central Arctic Ocean (continent) to the Barents Sea (interior Arctic Ocean), leading to less (more) clouds, which results in more (less) solar radiation received at the surface at the synoptic scale.

5. Summary and Conclusion

[25] This study has evaluated different surface radiative flux data sets in the Arctic Ocean, focusing on high temporal resolution at both the local and regional scales. More specifically, the following atmospheric parameters were examined: the (1) surface temperature; (2) surface downwelling shortwave radiative fluxes; and (3) surface downwelling longwave radiative fluxes from two satellite-based products (CASPR and ISCCP-FD), and two numerical weather prediction reanalyses (NCEP-R2 and ERA-40).

[26] For local comparisons, these data sets were evaluated against the SHEBA field measurements over the seasonal cycle. Comparisons suggest that the CASPR and NCEP-R2 surface temperatures are closest to the SHEBA observations. The CASPR and ISCCP-FD surface downward solar radiative fluxes are more accurate. The ERA-40 surface downward longwave radiative fluxes show reasonable agreement with the SHEBA measurements. In terms of the variations of the atmospheric parameters through particular storm events, the NCEP-R2, ISCCP-FD and ERA-40 well represent the observed temporal variability in the surface temperature, downward solar and longwave radiative fluxes, respectively. As mentioned previously, the SHEBA radiosonde data (i.e, the temperature profile) has been assimilated in the reanalyses (NCEP-R2 and ERA-40). By contrast, the CASPR surface temperature is determined by an empirical relationship between the clear sky surface

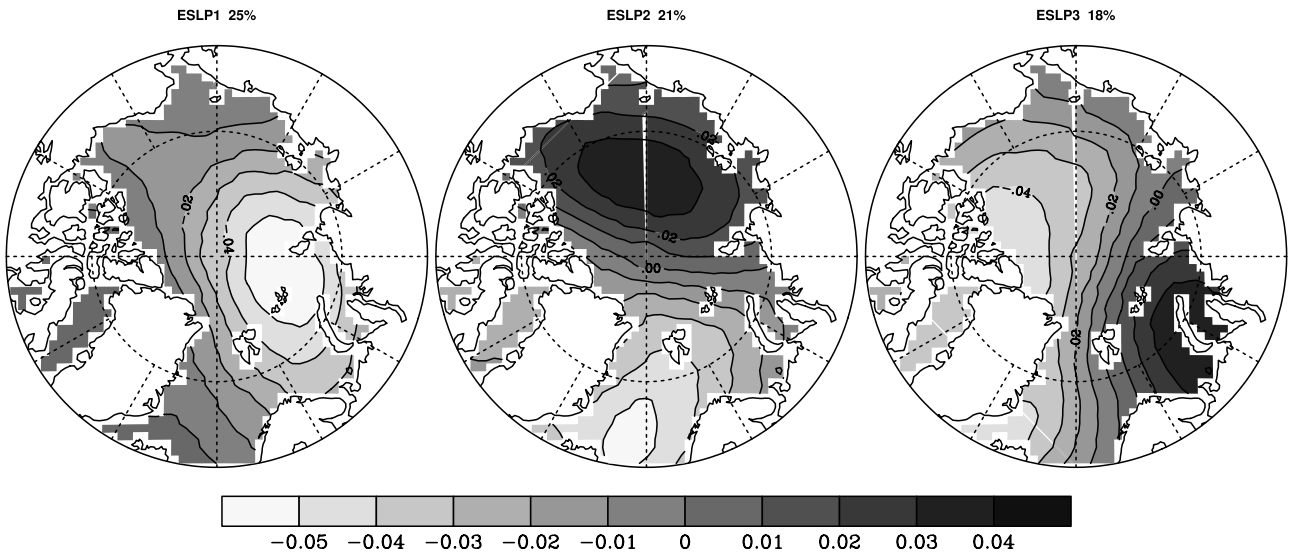

Figure 7. First three leading principal component loading patterns (EOFs) of the residual NCEP-R2 sea level pressure over the ocean north of 65°N after removing the seasonal cycle.

Table 5. Correlations Between the Principal Components of Figure 7 and the Principal Components of the NCEP-R2 of Figure 5[a]

NCEP-R2	SAT	SW	LW
ESLP1	**−0.28**	**0.45**	**−0.35**
ESLP2	0.06	−0.12	**−0.32**
ESLP3	**0.35**	0.19	**0.40**

[a]Correlations exceeding the 95% confidence level are in boldface.

skin temperature, wind speed, and solar zenith angle [*Key*, 2001], and the ISCCP-FD surface skin temperature is retrieved from the clear sky infrared (∼11 microns wavelength) brightness temperature by correcting for atmospheric emission and absorption of radiation, using data for the atmospheric temperature and humidity profiles, and for the fact that the surface infrared emissivity is less than one [*Zhang et al.*, 2004]. Thus it is not surprising that the reanalyses do well on the variability of the surface temperature relative to the satellite-based products (Table 1; Figures 1 and 2). However, the satellite-based products provide more accurate surface downward shortwave radiative fluxes relative to the reanalyses, because the satellite-based products have better cloud properties than the reanalyses (http://isccp.giss.nasa.gov/projects [*World Climate Research Programme*, 1999]). The ISCCP and CASPR clouds are observations of the real world (albeit with errors), while the reanalyses clouds are unvalidated model outputs. Sensitivity studies [*Zhang et al.*, 1995, 2004] also indicated that cloud fraction and sun elevation are more critical than other factors (i.e., surface albedo) for accurate downward shortwave radiative fluxes. Additionally, the ISCCP-FD and CASPR might have more realistic radiative transfer codes than the NCEP-R2 and ERA-40 [*Pinty et al.*, 2001]. Furthermore, our study indicates that the discrepancies of the monthly mean downwelling shortwave and longwave radiative fluxes among different data sets are smaller than earlier studies [e.g., *Zhang and Rothrock*, 1996; *Serreze et al.*, 1998]. This study shows that the satellite-based analyses may now provide the downward shortwave (longwave) radiative fluxes to within ∼10–40 (∼10–30) W/m^2. According to our validation results, the ERA-40 in particular may provide fluxes to within ∼10 W/m^2 when the observational data was assimilated. However, large discrepancies in surface radiative fluxes still exist between the NCEP-R2 and the SHEBA, and between the NCEP-R2 and ERA-40 due to different physical parameterizations and assimilation methods used in the NCEP-R2 and ERA-40.

[27] For regional comparisons, all data sets have consistent spatial/temporal patterns for each atmospheric parameter at the basin scale associated with the seasonal cycle (except the downward solar radiation in the CASPR). In terms of dominant spatial/temporal variability at the synoptic scale, all data sets show large surface temperature variability at Fram Strait. The downwelling solar radiative fluxes of the ISCCP-FD, NCEP-R2 and ERA-40 show similar spatial variability, while the downwelling longwave radiative fluxes of the CASPR, NCAP-R2 and ERA-40 show similar spatial variability. As shown in Figure 6, the principal component of the CASPR (ISCCP-FD) downward solar (longwave) radiative fluxes shows too large variability in the late spring and early fall (in summer) as compared with the others, which partly explains the aforementioned inconsistent spatial pattern between the CASPR (ISCCP-FD) and the others.

[28] Despite the aforementioned encouraging agreements, substantial temporal and spatial discrepancies are still found (1) between these data sets and the SHEBA field measurements and (2) among these data sets. For example, at the local scale, compared to the SHEBA measurements, the ISCCP-FD has too large bias for the surface temperature and the NCEP-R2 has too large biases for the downward solar and longwave radiative fluxes. At the basin scale, the dominant pattern associated with the synoptic variability of the CASPR and ISCCP-FD is not consistent with other data sets for the downward solar and longwave radiative fluxes respectively. Therefore more investigations are needed to understand the reasons leading to the differences between the satellite-based products, and between the reanalyses. At this stage, it is not entirely clear to what extent the results of this study can be generalized to infer which data set is superior to others and the most suitable data set for forcing sea ice models. Nevertheless, our results provide useful information for the ongoing Arctic System reanalysis project. Follow up model studies testing the impacts of these temporal and spatial discrepancies in different forcing data sets on basin-scale sea ice simulations will give us additional information for assessing which data set (or which combination of data sets) is optimal.

[29] **Acknowledgments.** This research is supported by the NASA polar program, NSF OPP-0240827, and the NOAA SEARCH program. We thank the SHEBA atmospheric surface flux group for help collecting and processing the data. The views, opinions, and findings contained in this research are those of the author(s) and should not be construed as an official NOAA or U.S. government position, policy, or decision.

References

Chiacchio, M., and J. A. Francis (2002), Evaluation of methods to estimate the surface downwelling longwave flux during Arctic winter, *J. Appl. Meteorol.*, *41*, 306–318.

Curry, J. A., W. B. Rossow, D. Randall, and J. L. Schramm (1996), Overview of Arctic cloud and radiative characteristics, *J. Clim.*, *9*, 1731–1764.

Curry, J. A., J. L. Schramm, A. Alam, R. Reeder, T. E. Arbetter, and P. Guest (2002), Evaluation of data sets used to force sea ice models in the Arctic Ocean, *J. Geophys. Res.*, *107*(C10), 8027, doi:10.1029/2000JC000466.

Ebert, E. E., and J. A. Curry (1993), An intermediate one-dimensional thermodynamic sea ice model for investigating ice-atmosphere interactions, *J. Geophys. Res.*, *98*, 10,085–10,109.

Intergovernmental Panel on Climate Change (2001), *Climate Change 2001: The Scientific Basis*, edited by J. T. Houghton et al., 944 pp., Cambridge Univ. Press, New York.

Kanamitsu, M., A. Kumar, H.-M. H. Juang, W. Wang, F. Yang, J. Schemm, S.-Y. Hong, P. Peng, W. Chen, and M. Ji (2002a), NCEP Dynamical Seasonal Forecast System 2000, *Bull. Am. Meteorol. Soc.*, *83*, 1019–1037.

Kanamitsu, M., W. Ebisuzaki, J. Woolen, J. Potter, and M. Fiorino (2002b), NCEP/DOE AMIP-II Reanalysis (R-2), *Bull. Am. Meteorol. Soc.*, *83*, 1631–1643.

Key, J. (2001), The Cloud and Surface Parameter Retrieval (CASPR) system for polar AVHRR data user's guide, report, 62 pp., Space Sci. and Eng. Cent. Univ. of Wis., Madison.

Key, J., and A. J. Schweiger (1998), Tools for atmospheric radiative transfer: Streamer and FluxNet, *Comput. Geosci.*, *24*, 443–451.

Perovich, D. K., et al. (1999), Year on ice gives climate insights, *Eos Trans. AGU*, *80*(41), 481, 485–486.

Persson, P., G. Ola, C. W. Fairall, E. L. Andreas, P. S. Guest, and D. K. Perovich (2002), Measurements near the atmospheric surface flux group tower at SHEBA: Near-surface conditions and surface energy budget, *J. Geophys. Res.*, *107*(C10), 8045, doi:10.1029/2000JC000705.

Pinty, B., et al. (2001), Radiation transfer model intercomparison (RAMI) exercise, *J. Geophys. Res.*, *106*, 11,937–11,956.

Randall, D., J. Curry, D. Battisti, G. Flato, R. Grumbine, S. Hakkinen, D. Martinson, R. Preller, J. Walsh, and J. Weatherly (1998), Status and outlook for large-scale of atmosphere-ice-ocean interactions in the Arctic, *Bull. Am. Meteorol. Soc.*, *79*, 197–219.

Rind, D., R. Healy, C. Parkinson, and D. G. Martinson (1995), The role of sea ice in $2 \times CO_2$ climate model sensitivity. part I: The total influence of sea ice thickness and extent, *J. Clim.*, *8*, 449–463.

Serreze, M. C., J. R. Key, J. E. Box, J. A. Maslanik, and K. Steffen (1998), A new monthly climatology of global radiation for the Arctic and comparisons with NCEP-NCAR reanalysis and ISCCP-C2 fields, *J. Clim.*, *11*, 121–136.

Uttal, T., et al. (2002), Surface heat budget of the Arctic Ocean, *Bull. Am. Meteorol. Soc.*, *83*, 255–275.

World Climate Research Programme (1999), *Proceedings of the Second WCRP International Conference on Reanalyses*, *WMO/TD 954*, Geneva, Switzerland.

Zhang, J., and D. Rothrock (1996), Surface downwelling radiative fluxes: Ice model sensitivities and data accuracies, paper presented at the Workshop on Polar Processes in Global Climate, Am. Meteorol. Soc., Cancun, Mexico, 13–15 Nov.

Zhang, Y.-C., W. B. Rossow, and A. A. Lacis (1995), Calculation of surface and top of atmosphere radiative fluxes from physical quantities based on ISCCP data sets: 1. Method and sensitivity to input data uncertainties, *J. Geophys. Res.*, *100*, 1149–1165.

Zhang, Y.-C., W. B. Rossow, A. A. Lacis, V. Oinas, and M. I. Mishchenko (2004), Calculation of radiative fluxes from the surface to top of atmosphere based on ISCCP and other global data sets: Refinements of the radiative transfer model and the input data, *J. Geophys. Res.*, *109*, D19105, doi:10.1029/2003JD004457.

J. A. Curry and J. Liu, School of Earth and Atmospheric Sciences, Georgia Institute of Technology, Atlanta, GA 30332-0340, USA. (curryja@eas.gatech.edu; jliu@eas.gatech.edu)

J. R. Key, Office of Research and Applications, NOAA National Environmental Satellite, Data and Information Service, 1225 West Dayton Street, Madison, WI 53706, USA. (jkey@ssec.wisc.edu)

W. B. Rossow, NASA/Goddard Institute for Space Studies, 2880 Broadway, New York, NY 10025, USA. (wrossow@giss.nasa.gov)

X. Wang, Cooperative Institute of Meteorological Satellite Studies, University of Wisconsin, 1225 West Dayton Street, Madison, WI 53706, USA. (xuanjiw@ssec.wisc.edu)